Approaching the capacity limit of lithium cobalt oxide in lithium ion batteries *via* lanthanum and aluminum doping

Qi Liu[1,2,+,#], Xin Su[2,+,*], Dan Lei[3,+], Yan Qin[2], Jianguo Wen[4], Fangmin Guo[1], Yimin A Wu[4], Yangchun Rong[1], Ronghui Kou[1], Xianghui Xiao[1], Frederic Aguesse[1], Javier Bareño[1], Yang Ren[1,*], Wenquan Lu[2], Yangxing Li[3,*]

[1]X-ray Science Division, Advanced Photon Source, Argonne National Laboratory, 9700 South Cass Avenue, Argonne, Illinois 60439, USA

[2]Chemical Science and Engineering Division, Argonne National Laboratory, 9700 South Cass Avenue, Argonne, Illinois 60439, USA

[3]Central Research Institute, Huawei Technologies Co., Ltd., Longgang District, Shenzhen, 518129, China

[4]Center for Nanoscale Materials, Argonne National Laboratory, 9700 South Cass Avenue, Argonne, Illinois 60439, USA

[+]Q. Liu, X. Su and D. Lei made equal contributions to the manuscript.

[#]Present address: Department of Physics, City University of Hong Kong, Hong Kong, China.

[*]Corresponding author: Yangxing Li (li.yangxing@huawei.com), Yang Ren (ren@aps.anl.gov), Xin Su (xin.su@eaglepicher.com)

Abstract

Lithium cobalt oxides (LiCoO$_2$) possess a high theoretical specific capacity of 274 mAh/g. However, cycling LiCoO$_2$-based batteries to voltages greater than 4.35 V *vs.* Li/Li$^+$ causes significant structural instability and severe capacity fade. Consequently, commercial LiCoO$_2$ exhibits a maximum capacity of only ~165 mAh/g. Here we develop a doping technique to tackle this long-standing issue of instability and thus increase the capacity of LiCoO$_2$. La and Al are concurrently doped into Co-containing precursors, followed by high-temperature calcination with lithium carbonate. The dopants are found to reside in the crystal lattice of LiCoO$_2$, where La works as a pillar to increase the *c*-axis distance and Al as a positively charged center, facilitating Li$^+$ diffusion, stabilizing the structure and suppressing the phase transition during cycling, even at a high cut-off voltage of 4.5 V. This doped LiCoO$_2$ displays an exceptionally high capacity of 190 mAh/g, cyclability with 96% capacity retention over 50 cycles and significantly enhanced rate capability.

Introduction

Because of their high energy density, lithium ion batteries (LIBs) have become a rapidly growing energy storage technology with wide applications in mobile phones, portable electronics and electric cars[1-5]. Cathode materials are one major performance-limiting factor for cell energy and power density. There are many advanced cathode materials such as Li, Mn-rich and Ni-rich transition metal oxides, and much progress has been made to improve their performance[6-8]. However, these materials face significant issues such as voltage and capacity fading as well as structural and thermodynamic instability, which have so far prevented their commercialization[8, 9].

Among the commercialized cathode materials, $LiCoO_2$ is the most successful for portable devices; for example, it is used in the majority of smart phones. However, commercial $LiCoO_2$-based batteries generally utilize only a little more than half its theoretical capacity. Such a large irreversible capacity is mainly attributed the presence of phase transitions. Studies have shown that $LiCoO_2$ experiences a series of phase transitions during the lithium insertion/deinsertion processes[10-12]. Initially, there is an insulator-metal phase transition in the low-voltage region. Then, when charging to 4.2 V, approximately 50% of the Li^+ ions are removed and the material experiences an order/disorder transition from the hexagonal structure (O3 phase, R-3m space group, 3CoO_2 slabs in a unit cell, both Li^+ and Co^+ occupy the octahedral sites) to a monoclinic structure (C2/m phase group, Li occupying 2a and 4c sites, Co occupying 2b and 4c sites, and three oxygens occupying 4c sites), and then back to a hexagonal structure (O3 phase). When charging to above 4.5V, the cathode undergoes another transition from the O3 phase to a H1-3 phase (R-3m group, 6 CoO_2 slabs in a unit cell, Li occupying the 3a sites, Co and two oxygens occupying the 6c sites) before the emergence of O1 phase (1 CoO_2 slab in a unit cell)[11]. These phase transitions are quite reversible, but the order/disorder transition substantially lowers the Li^+

diffusivity and the transition to the H1-3 phase severely stresses the structure, generating mechanical strains and micro-cracks between and within the particles. These phase transitions, coupled with the decreased Li^+ diffusivity and increased mechanical stress, lead to dramatic capacity fading in the deeply charged Li_xCoO_2. Accordingly, the charging voltage was restricted to 4.2 V in the early development stage of commercial $LiCoO_2$-based batteries[13].

In order to maintain structural integrity and stable electrochemical performance, substantial efforts towards improving the $LiCoO_2$ capacity have been made *via* various techniques such as doping with various metals and surface modification by coating with MgO[14], Al_2O_3[15], TiO_2[15] and ZrO_2[15,16] *etc*. Among these techniques, doping with different elements including Mg[17-19], Zr[19,20], Al[21,22], Ni[23], Fe[24], Cr[25], Mn[26] and Ti[27] have been employed to suppress the order/disorder transition, with varying degrees of success. This has led to an improvement of $LiCoO_2$-based commercial LIBs from 4.2 V in the 1990s to 4.35 V at present, achieving a delivered capacity of 165 mAh/g. However, this is still far below the capacity limit. For higher capacity, one has to utilize more lithium in the insertion/deinsertion processes by pushing $LiCoO_2$ to work at higher voltages, where it is more challenging to maintain the structural integrity and improve Li^+ diffusivity.

In this work, we dope the $LiCoO_2$ cathode with two elements concurrently, lanthanum and aluminum, to address the above-mentioned issues. The larger-diameter La cations function as a pillar and effectively increase the *c*-axis spacing, leading to a significant increase in Li^+ diffusivity. The smaller-diameter Al cations serve as positively charged centers that disrupt and suspend the order-disorder transitions and H1-3 phase transition during cycling. Compared with pristine $LiCoO_2$, the co-doped $LiCoO_2$ can work at a cut-off voltage as high as 4.5 V *vs.* Li/Li^+, significantly improving its capacity retention from 84% to 96% with an exceptionally high capacity of 190 mAh/g at C/3.

Characterization of the cathode materials

The co-doping approach starts with the preparation of La- and Al-co-doped cobalt carbonate ($CoCO_3$) *via* a controlled liquid-state crystallization. In a subsequent annealing, co-doped Co_3O_4 is formed as a precursor of the doped $LiCoO_2$ in which the occupation of La and Al in Co sites is inherited. Finally, the co-doped $LiCoO_2$ (D-LCO) is synthesized by calcinating this precursor with Li_2CO_3 at 1050 °C for 12 h. The chemical composition ratio of La:Al:Co was measured by inductively coupled plasma mass spectrometry (ICP) and estimated to be 1:2:1000. The schematic structures of the co-doped $CoCO_3$ and Co_3O_4 and the D-LCO are shown in Fig. 1a. In a typical doping method, the dopants usually diffuse into the $LiCoO_2$ layer structure and substitute the Co atoms *via* a solid-state reaction at high temperature[17, 18, 25]. However, this dopant diffusion in solid-state is very limited and a large amount of the dopants is diverted to coating dots on a submicron or micron scale.

TEM images of both D-LCO (Fig. 1b) and pristine LCO (P-LCO) (Supplementary Fig.1) show pure, continuous lattice fringes with a *d*-spacing of 4.70 nm. In high-angle annular dark-field (HAADF) images of the D-LCO (Supplementary Fig.2), the location of the La can be clearly seen. In Supplementary Fig.2 (a), the dots show different contrast in the transition metal layers with the La looking brighter due to the Z-contrast in the HAADF images, showing that the substitution doping is working well. However, some La dopants also can be seen in Li layers in Supplementary Fig.2 (a, b) due to the cation mixing. In order to distinguish the subtle difference in crystal structure between the P-LCO and D-LCO, high-resolution X-ray diffraction (HRXRD) measurements were carried out at the Advanced Photon Source (APS), clearly showing that the *c* lattice parameter increases by 0.03% from 14.0545 Å in P-LCO to 14.0588 Å in D-LCO, while the *a* lattice

parameter decreases by 0.01% from 2.8159 Å to 2.8156 Å. The increased c lattice parameter and decreased a lattice parameter in D-LCO are further verified by the (003) peak shifting to lower angle compared with that of P-LCO (Fig. 1e) and by the merging of the (31-1) and (01,20) peaks (Fig. 1f). Further inspection of the HRXRD patterns indicates that the co-element doping also improves the $LiCoO_2$ crystallinity, as evidenced by the sharper peaks in D-LCO compared with P-LCO.

At the same time, our HRXRD results clearly show that there is a small decrease of intensity ratio between (003) and (104), indicating that a small amount of La is located in the Li site due to cation mixing, consistent with our HAADF images (Supplemental Fig.2). Our SEM images show that both P-LCO and D-LCO are made up of 15~25 μm particles (Fig. 1g & Supplementary Fig. 3). In addition, the effect of Co dissolution was investigated according to the approach of Ref. 28, showing that the content of Co ions in solution after storing the half cells with Li metal as the anode at 60 °C for 14 days was 4.2 ppm for D-LCO and 91.1 ppm for P-LCO. The loss of Co for these two electrodes was 0.07% and 1.51%, respectively (Supplementary Table 1). Obviously, the doping mitigates the Co ion dissolution at the increased cut-off voltage, which can be ascribed to the improved structural stability. Though Co dissolution does occur in the system, it is negligible in the dry solutions without invasion of water[29].

Electrochemical performance and phase transition

The electrochemical results clearly show that the introduction of a small amount of La and Al can have a profound effect on the performance. As shown in Fig. 2a, a specific capacity of 190 mAhg^{-1} has been achieved at 0.1 C for the D-LCO with a cut-off voltage of 4.5 V, which amounts to 70% of the theoretical capacity of $LiCoO_2$. In comparison, although P-LCO can also deliver a

high specific capacity of 190 mAh/g at 0.1 C (Fig. 2b), the rate and cycle performance is quite different. When working at a higher rate such as 2 C, the D-LCO can deliver 167 mAhg^{-1}, 14 mAhg^{-1} higher than that of P-LCO (Fig. 2c). Importantly, at 25 °C the capacity retention of D-LCO is 96% over 50 cycles with a cut-off voltage of 4.5 V, compared to 84% for P-LCO (Fig.2d). Even at an elevated temperature of ~45 °C or in a full-cell configuration using graphite as the anode and the D-LCO and P-LCO as the cathode, the doping effect is obvious and the cycling performance is much better in D-LCO than P-LCO (Supplementary Fig. 4 & Fig. 5). Moreover, AC impedance spectra clearly show that D-LCO exhibits a smaller resistance than P-LCO and partially explains the reason for the improved performance (Supplementary Fig. 6). To the best of our knowledge, this is the highest aggregate performance ever reported for $LiCoO_2$. Considering that Co dissolution is not significant in the D-LCO system, the major reason could be ascribed to the structural aspects as described in detailed below. Such an improvement suggests that not only the crystal structural stability of D-LCO has been improved but the Li diffusivity has also been increased.

Results for dQ/dV during the formation cycle can be used to investigate the phase transition behavior. Notably, our dQ/dV curve for P-LCO shows that three distinct phase transitions occur at 4.1 V, 4.2 V and 4.46 V vs Li/Li$^+$ when charging to 4.5 V (Fig. 2e). As reported in a previous study, when $LiCoO_2$ is delithiated, the material experiences a series of phase transitions[30]. Initially, there is an insulator-metal transition in the low voltage region associated with a first-order phase transition with a coexistence region. As the material continues to be delithiated and when a half of Li$^+$ is removed from $LiCoO_2$, the cathode experiences an order/disorder transition, which drives the phase transition from the hexagonal structure (O3) to the monoclinic structure. Further delithiated LCO tends to experience the O3-(H1-3)-O1 phase transition[11, 31]. As seen in Fig. 2e,

two minor peaks appear at 4.1 V and 4.2 V, which are associated with order/disorder transitions near $Li_{0.5}CoO_2$. The peak at 4.46 V is likely due to the appearance of the H1-3 phase. However, no such phase transition peaks are seen for D-LCO (Fig. 2f), indicating that the order/disorder transition has been eliminated and the H1-3 phase transition has been suppressed. In our designed D-LCO, the Al is smaller than Co but has a charge of 3+, so it could be serve as a fixed-charge center to block the rearrangement of lithium vacancies[32]. The absence of a phase transition further confirms that Al is successfully introduced into the D-LCO lattice, suppressing the phase transitions with a cut-off voltage of 4.5 V. Since all performance changes should be rooted in the material structure and the lithium insertion/deinsertion processes, *in situ* synchrotron high-energy X-ray diffraction (HEXRD) and galvanostatic intermittent titration technique (GITT) characterizations were conducted to further understand the structure evolution and lithium insertion/deinsertion mechanism, as described in the next section.

In situ synchrotron HEXRD characterization

To further elucidate the doping effects, *in situ* HEXRD measurements on the P-LCO and D-LCO cells were performed at the Advanced Photon Source (APS). As seen in Fig. 3a, the evolution of the HEXRD patterns correlates well with the electrochemical process. The symmetric structure evolution behavior indicates that the insertion/deinsertion processes for the D-LCO are completely reversible when cycled at the cut-off voltage of 4.5 V. The highly reversible structure change is consistent with the observed electrochemical process (Fig. 2b and Fig. 2d), explaining why the D-LCO exhibits highly reversible capacity and nearly 100% coulombic efficiency. The P-LCO has quite different structural evolution compared with that of D-LCO during the charging/discharging processes (Fig. 3a and Supplementary Fig.7).

First, the D-LCO exhibits a single-phase solid-solution insertion/deinsertion behavior after the initial insulator-metal transition highlighted by the black dashed circle in Fig.3a, while a series of phase transitions can be clearly identified for the P-LCO as fully revealed in Supplementary Fig.7 (a). As shown in Fig. 3d, the intensity and position of the (015) peaks for the D-LCO evolves smoothly and no new peaks emerge during the charge/discharge process, indicating that the order/disorder phase transition between hexagonal and monoclinic phases has been successfully suppressed, consistent with our dQ/dV results (Fig. 2f). In contrast, during the charge process, the (015) peaks of the P-LCO electrode split into two components with the appearance of lighter-red-color peaks when the charging reaches ~4.1 V, which can be ascribed to the phase transition from hexagonal Li_xCoO_2 to monoclinic Li_xCoO_2. Then the two peaks merge together with the disappearance of the lighter-red-color peaks at around ~4.2 V, indicating that further delithiation drives the phase transition from the monoclinic phase back to the hexagonal phase (order/disorder transition). A similar evolution is observed for other characteristic peaks such as (104), (107) and (018) (Supplementary Fig.7), which is also consistent with our dQ/dV results on the P-LCO (Fig. 2e). Since the single-element La-doped LCO also experiences a series of phase transitions (Supplementary Fig.8a), we can expect that it is the introduction of Al that suppresses the phase transition. Whereas the order/disorder transition the lowers Li^+ diffusivity and the H1-3 phase transition leads to structural distortion[33], the single-phase transition process in D-LCO offers a significant advantage – the transformation path is much more facile and homogeneous than that of P-LCO with multiple phase transitions[34]. Thus, the stresses and mechanical degradation of the material are significantly reduced during cycling.

Secondly, the unit cell volume change of D-LCO is smaller than that of P-LCO. As seen in Fig. 3b and Fig. 3c, the position of the (003) peak first shifts to a lower 2-theta angle, then shifts

back to the higher 2-theta angle, indicating an initial steady increase of the c-lattice parameter with a subsequent decrease. The initial increase can be attributed to the increased electrostatic repulsion between adjacent CoO_2 layers due to the removal of Li^+, while the subsequent decrease results from the CoO_2 layers shifting due to deep delithiation[35]. The evolution of the position of the (003) peak for P-LCO shows the same trend but the amplitude of the shift is greater than that of D-LCO, as marked by arrows in Fig 3b and Fig.3c. With the changes in the (003) peaks, the unit cell volume also changes (Fig. 3f). For P-LCO, the unit cell volume increases from 96.50 $Å^3$ to 98.90 $Å^3$, after which it decreases to 95.31 $Å^3$. The maximum volume change is 3.63% (Supplementary Fig.7). On the other hand, the unit cell volume of D-LCO first increases from 96.54 $Å^3$ to 98.48 $Å^3$, and then decreases to 95.56 $Å^3$ in the fully charged state. The maximum volume change for D-LCO is 2.97%, which is smaller than that for P-LCO. As a result, the improved performance of the D-LCO can be explained by the absence of phase transitions (including the order/disorder transition) and the smaller volume change results in lower structural distortion and reduced mechanical degradation of the material.

Li ion diffusion coefficient determination

The lithium ion diffusion coefficients for P-LCO and D-LCO were determined *via* GITT (Supplementary Table 2). As seen in Figs. 4a, 4c and 4e, the lithium ion diffusion coefficient for the P-LCO was determined to be 6.5×10^{-11} cm^2/s at the initial charging stage and 4.5×10^{-12} cm^2/s at the final discharge stage. In comparison, the lithium ion diffusion coefficient of D-LCO is 1.2×10^{-10} cm^2/s at the initial charging stage and 4.7×10^{-11} cm^2/s at the final discharging stage according to Figs. 4b, 4d and 4f. Note that the values for D-LCO are twice those for P-LCO at the initial charging stage and 10 times greater at the final discharging stage. In addition, the GITT

result shows that the lithium ion diffusion coefficient for single-element La-doped LCO is much higher than that of P-LCO, reaching almost the same value as that of D-LCO (Supplementary Fig.8). These results clearly verify that the co-doping can provide a beneficial increase of Li^+ diffusivity for D-LCO, which is partially associated with the introduction of La. The activation barrier for the diffusion depends on the spacing of the lithium layer, and the increase of the layer distance along the c-axis significantly increases the Li^+ diffusivity. As evidenced by the HRXRD and HAADF (Supplementary Fig.2), the larger La ions in the structure effectively enlarge the c-axis spacing and facilitate the Li^+ diffusion. In addition, since the introduction of Al suppresses the order/disorder transition, the Al doping also partially contributes to the increase of the Li^+ diffusivity of D-LCO, since the phase transition suppression and structural stabilization are always coupled with the increase of Li^+ diffusivity[33]. Further work is in progress to investigate the dependence of Li^+ diffusivity on the doping amounts of Al and La.

Structural stability during cycling

Long-term cyclability at the high cut-off voltage like 4.5 V is always challenging for $LiCoO_2$. As discussed above, our designed D-LCO with the absence of an order/disorder transition, less stress variation and increased Li^+ diffusivity makes it possible to achieve 96% capacity retention over 50 cycles when cycling at 4.5 V. A hybrid pulse power characterization (HPPC) was carried out to study the area specific impedance (ASI) change during cycling. As seen in Fig. 5a and Fig. 5b, the impedance of D-LCO increases more slowly than that of P-LCO during cycling, which can be attributed to the reduced stress and suppression of phase transitions (including the order/disorder transition). In contrast, the phase transition at high voltage associated with larger mechanical stress must undoubtedly cause mechanical failure of the P-LCO and thus fracture the

solid electrolyte interface (SEI). So, the broken and rebuilt SEI on P-LCO would tend to increase the ASI during cycling. The phase transition is believed to severely stress the structure. Therefore, mitigating the phase transition, especially the H1-3 transition, can significantly reduce the crystal volume and stress expansion when cycling to high voltage. Consequently, we can find various tiny cracks on the surface of the P-LCO particles but find none for the D-LCO particles after long-term cycling at 4.5 V (Fig. 6a and Fig. 6b). This distinctly different behavior further confirms that the stress evolution of $LiCoO_2$ associated with phase transitions during cycling is effectively mitigated by the La and Al co-doping. In summary, the La and Al co-doped into the $LiCoO_2$ layers not only stabilize the crystal structure and enhance the d-spacing along the c-axis, but also serve as positive charged centers, facilitating the Li^+ diffusion and suppressing the phase transition.

Conclusions

At the present time, doping is considered to be an effective way to improve the electrochemical performance of $LiCoO_2$. However, most approaches have only partially improved the structural stability of the material and have met with limited degree of success. Although the upper cut-off voltage of $LiCoO_2$ can be increased from 4.2 V to 4.35 V, working at a higher voltage such as 4.5 V typically inflicts a heavy penalty on the cycling performance[36]. In this work, we have demonstrated that the La- and Al- doping strategy on a Co-containing precursor can improve the structure stability and Li^+ diffusivity of $LiCoO_2$. Such a doped $LiCoO_2$ can achieve 96% capacity retention over 50 cycles at a cut-off voltage of 4.5 V. Importantly, commercially $LiCoO_2$-based batteries never work properly at 4.5 V. Our approach, with the potential to be easily scaled up, may make these D-LCO batteries commercially feasible. Finally, considering that the other commercial cathode materials such as $LiNi_xMn_yCo_zO_2$ (x+y+z=1) possess a similar layered

structure, our method could suggest an approach to create a wide variety of high-voltage and high-energy density layered cathode materials for LIBs.

Methods

Materials synthesis

In this synthesis, reagent-grade $CoSO_4$, Na_2CO_3 and compounds of Al (a metal that has a radius similar to Co^{3+}/Co^{4+}) and La (a transition-metal that has a larger radius than Co^{3+}/Co^{4+}) were used as starting materials to prepare Al and La co-doped $CoCO_3$ powder *via* a controlled crystallization method at a specific pH value. Then, the mixture of the Al and La co-doped $CoCO_3$ and the compound of Al were calcined at 800 °C for 6 h to form Al and La co-doped Co_3O_4 precursor. The P-LCO and D-LCO powders were synthesized by heat-treatment of a stoichiometric mixture of Li_2CO_3 and Co_3O_4 at 1050 °C for 12 h. The chemical composition ratio of La: Al: Co was measured via ICP (ICP-MS, Agilent 5100 ICP-OES) and is estimated to be 1:2:1000.

Materials Characterization

The particle size and size distribution of P-LCO and D-LCO powder were evaluated using a Cilas 1090 particle size analyzer. The amount of Co dissolution was measured by ICP-MS (Agilent 5100 ICP-OES). The surface morphologies and compositions of P-LCO and D-LCO powder before and after the cycling test were characterized using a Hitachi S-4700 at 10 KV scanning electron microscope (SEM). High-resolution transmission electron microscope (TEM) images and the HAADF images were conducted on a FEI Talos F200X scanning transmission electron microscope (STEM) with accelerate voltage of 200 kV at the Center for Nanoscale

Materials, Argonne National Laboratory (ANL). The crystal structures of the samples were characterized *via* HRXRD at the beamline 11-BM (λ= 0.4593 Å) of APS, ANL. The samples were loaded in 0.8 mm Kapton capillaries for the measurements.

Electrode preparation and electrochemical methods

The electrodes with P-LCO or D-LCO powder was prepared by spreading a slurry composed of 90% LCO, 5% poly vinylidene difluoride (PVDF) and 5% carbon black onto an alumina foil and then dried at 75 °C in a vacuum for 24 h. The coatings of the electrodes on Al foil were kept at ~10 mg/cm^2 with 30% porosity. 2032-type coin cells were made up of the as-prepared electrodes as the cathode, lithium metal or graphite as the anode, and the solution of 1.2 mol/L LiPF$_6$ in ethylene carbonate (EC)/ethyl methyl carbonate (EMC) (3/7 by weight) as the electrolyte in all the cells.

Galvanostatic cycling tests of the home-made coin cells were conducted using a MACCOR battery cycler. The initial three formation cycles of the cells were carried out from 3.0 V to 4.5 V vs Li/Li$^+$ under a constant current of 0.1 C. After that, the cells were tested at rates of C/5, C/3, C/2, 1 C, and 2 C from 3.0 V to 4.5 V. Finally, the cycling tests of the cells were carried out using a rate of C/3. The GITT measurements of the electrodes using P-LCO, D-LCO and single-element La-doped LCO powder were conducted using a MACCOR battery cycler at room temperature. The test procedure was as follows: a 10-min galvanostatic charge pulse (0.1 C) was applied to the cells, followed by 2 h of relaxation time without any current being passed through the cell. The cycle, consisting of a charge pulse and a relaxation period, was applied to the cell until its voltage increased to 4.5 V vs Li/Li$^+$. Then a discharge pulse (0.1 C, 10 min) was applied to the cells, followed by a 2 h relaxation period without any current flowing through the cell. The cycle was applied to the cells until its voltage reached 3.0 V vs Li/Li$^+$. Two charging-discharging cycles from

3.0 V to 4.5 V vs Li/Li$^+$ for GITT measurement were carried out on all electrodes. The HPPC was conducted during the cycling test, in which a 10-s 2 C discharge pulse and a 1.5 C regenerative charge pulse current were applied to the cells. There were 40-s rest periods between discharge and regenerative pulses. The pulse profiles were measured at every 10% depth of discharge (DOD). The area specific impedance (ASI) as a function of depth-of-discharge was established by calculating the voltage changes during pulses.

In situ HEXRD characterization.

In situ HEXRD measurements were performed using beamline 11-ID-C at the APS, ANL. A monochromator with a Si (113) single crystal was used to provide an X-ray beam with an energy of 105.7 keV. A high-energy x-ray beam with a beam size of 0.2 mm × 0.2 mm and a wavelength of 0.1173 Å was used to obtain two-dimensional diffraction patterns in the transmission geometry. XRD patterns were collected with a Perkin-Elmer large-area detector placed at 1800 mm away the samples. In a typical _in situ_ experiment, the home-made coin cells (LiCoO$_2$ on Al) were discharged/charged with a constant current of ~0.1 C. The diffraction data for each sample were collected every 360 s. The obtained 2D diffraction patterns were calibrated using a standard CeO$_2$ sample and converted to 1D patterns using Fit$_2$D software. For our obtained XRD data, the general structure analysis software (GSAS) program was used to fit the observed diffraction patterns and obtain the lattice parameters.

Data availability

The data that support the findings of this study are available from the corresponding authors upon request.

Acknowledgements

Author contributions

Y.L. and W.L. conceived the idea. Q.L., X.S. and D.L. designed and performed the experiments. X.S., Q.L., and Y.Q. performed the electrochemical characterization. Q.L., X.S., Y.R., F.G., R.K., X.X., and Y.Re. carried out the *in situ* and *ex situ* synchrotron measurements. Q.L., Y. R. and Y.Re. analyzed and interpreted the synchrotron XRD data. D.L. and X.S. performed the SEM work. J.W., D.L., and Y.W performed the STEM and the HAADF images. F.A. and J.B. contributed to discussions and interpretation of the electrochemical data. Q.L., D.L., X.S., Y.Re., W.L, and Y.L. wrote the paper. The project was supervised by Y.L., W.L and Y.Re. All authors discussed the results and reviewed the manuscript.

Competing interests

The authors declare no competing financial and non-financial interests.

References

1. Sun, Y. *et al*. High-capacity battery cathode prelithiation to offset initial lithium loss. *Nat. Energy* **1**, 15008 (2016).

2. Pang, Q., Liang, X., Kwok, C.Y.& Nazar, L.F. Advances in lithium–sulfur batteries based on multifunctional cathodes and electrolytes. *Nat. Energy* **1**, 16132 (2016).

3. Tarascon, J.M.& Armand, M. Issues and challenges facing rechargeable lithium batteries. *Nature* **414**, 359-367 (2001).

4. Nitta, N., Wu, F., Lee, J.T.& Yushin, G. Li-ion battery materials: present and future. *Mater. Today* **18**, 252-264 (2015).

5. Etacheri, V., Marom, R., Elazari, R., Salitra, G.& Aurbach, D. Challenges in the development of advanced Li-ion batteries: a review. *Energy Environ. Sci.* **4**, 3243-3262 (2011).

6. Kim, J.& Manthiram, A. A manganese oxyiodide cathode for rechargeable lithium batteries. Nature 390, 265-267 (1997).

7. Lin, F. *et al*. Surface reconstruction and chemical evolution of stoichiometric layered cathode materials for lithium-ion batteries. *Nat. Commun.* **5**, 3529 (2014).

8. Zheng, F. *et al*. Nanoscale surface modification of lithium-rich layered-oxide composite cathodes for suppressing voltage fade. *Angew. Chem. Int. Ed.* **54**, 13058-13062 (2015).

9. Qiu, B. *et al*. Gas–solid interfacial modification of oxygen activity in layered oxide cathodes for lithium-ion batteries. *Nat. Commun.* **7**, 12108 (2016).

10. Amatucci, G.G., Tarascon, J.M.& Klein, L.C. CoO_2, the end member of the Li_xCoO_2 solid solution. *J.Electrochem.Soc.* **143**, 1114-1123 (1996).

11. Van der Ven, A., Aydinol, M.K., Ceder, G., Kresse, G.& Hafner, J. First-principles investigation of phase stability in Li_xCoO_2. *Phys. Rev. B* **58**, 2975-2987 (1998).

12. Mizushima, K., Jones, P., Wiseman, P.& Goodenough, J.B. Li_xCoO_2 (0< x≤1): A new cathode material for batteries of high energy density. *Mater. Res. Bull.* **15**, 783-789 (1980).

13. Whittingham, M.S. Lithium batteries and cathode materials. *Chem.Rev.* **104**, 4271-4301 (2004).

14. Shim, J.H., Lee, S. &Park, S.S. Effects of MgO coating on the structural and electrochemical characteristics of LiCoO2 as cathode materials for lithium ion battery. *Chem.Mater.* **26**, 2537-2543 (2014).

15. Kannan, A.M., Rabenberg, L. &Manthiram, A. High capacity surface-modified LiCoO2 cathodes for lithium-ion batteries. *Electrochem. Solid-state Lett.* **6(1)**, A16-A18 (2003).

16. Chen, Z.& Dahn, J.R. Improving the capacity retention of LiCoO2 cycled to 4.5V by heat-treatment. *Electrochem. Solid-state Lett.* **7(1)**, A11-A14 (2004).

17. Shim, J.-H., Lee, J., Han, S.Y.& Lee, S. Synergistic effects of coating and doping for lithium ion battery cathode materials: synthesis and characterization of lithium titanate-coated $LiCoO_2$ with Mg doping. *Electrochim. Acta* **186**, 201-208 (2015).

18. Levasseur, S., Ménétrier, M.& Delmas, C. On the $Li_xCo_{1−y}Mg_yO_2$ system upon deintercalation: electrochemical, electronic properties and ^{7}Li MAS NMR studies. *J. Power Sources* **112,** 419-427 (2002).

19. Nobili, F. *et al*. Sol–gel synthesis and electrochemical characterization of Mg-/Zr-doped $LiCoO_2$ cathodes for Li-ion batteries. *J. Power Sources* **197**, 276-284 (2012).

20. Kim, H.-S., Ko, T.-K., Na, B.-K., Cho, W.I.& Chao, B.W. Electrochemical properties of $LiM_xCo_{1−x}O_2$ [M = Mg, Zr] prepared by sol–gel process. *J. Power Sources* **138**, 232-239 (2004).

21. Jang, Y.-I. *et al*. Synthesis and characterization of $LiAl_yCo_{1−y}O_2$ and $LiAl_yNi_{1−y}O_2$. *J. Power Sources* **81–82**, 589-593 (1999).

22. Ceder, G. *et al*. Identification of cathode materials for lithium batteries guided by first-principles calculations. *Nature* **392**, 694-696 (1998).

23. Adipranoto, D.S. *et al*. Neutron diffraction studies on structural effect for Ni-doping in $LiCo_{1-x}Ni_xO_2$. *Solid State Ion.* **262**, 92-97 (2014).

24. Alcántara, R. *et al*. X-ray diffraction, ^{57}Fe Mössbauer and step potential electrochemical spectroscopy study of $LiFe_yCo_{1-y}O_2$ compounds. *J. Power Sources* **81–82**, 547-553 (1999).

25. Madhavi, S., Subba Rao, G.V., Chowdari, B.V.R.& Li, S.F.Y. Effect of Cr dopant on the cathodic behavior of $LiCoO_2$. *Electrochim. Acta* **48**, 219-226 (2002).

26. Stoyanova, R., Zhecheva, E.& Zarkova, L. Effect of Mn-substitution for Co on the crystal structure and acid delithiation of $LiMn_yCo_{1-y}O_2$ solid solutions. *Solid State Ion.* **73**, 233-240 (1994).

27. Gopukumar, S., Jeong, Y.& Kim, K.B. Synthesis and electrochemical performance of tetravalent doped $LiCoO_2$ in lithium rechargeable cells. *Solid State Ion.* **159**, 223-232 (2003).

28. Sun, Y.K., Han, J.M., Myung, S.T., Lee, S.W.& Amine, K. Significant improvement of high voltage cycling behavior AlF_3-coated $LiCoO_2$ cathode. *Electrochem. Commun.* **8**, 821-826 (2006).

29. Markevich, E., Salitra, G.& Aurbach, D. Influence of the PVdF binder on the stability of $LiCoO_2$ electrodes. *Electrochem. Commun.* **7**, 1298-1304 (2005).

30. Reimers, J.N.& Dahn, J. Electrochemical and in situ X-ray diffraction studies of lithium intercalation in Li_xCoO_2. *J. Electrochem. Soc.* **139**, 2091-2097 (1992).

31. Chen, Z., Lu, Z.& Dahn, J.R. Staging phase transitions in Li_xCoO_2. *J. Electrochem. Soc.* **149**, A1604-A1609 (2002).

32. Wolverton, C.& Zunger, A. First-principles prediction of vacancy order-disorder and intercalation battery voltages in Li_xCoO_2. *Phys. Rev. Lett* **81**, 606 (1998).

33. Xia, H., Lu, L., Meng, S.Y.& Ceder, G. Phase transitions and high-voltage electrochemical behavior of $LiCoO_2$ thin films grown by pulsed laser deposition. *J. Electrochem. Soc.* **154**, A337-A342 (2007).

34. Malik, R., Zhou, F.& Ceder, G. Kinetics of non-equilibrium lithium incorporation in $LiFePO_4$. *Nat. Mater.* **10**, 587-590 (2011).

35. Yin, R.-Z. *et al*. In situ XRD investigation and thermal properties of Mg doped $LiCoO_2$ for lithium ion batteries. *J. Electrochem. Soc.* **159**, A253-A258 (2012).

36. Amatucci, G.G., Tarascon, J.M.& Klein, L.C. Cobalt dissolution in $LiCoO_2$-based non-aqueous rechargeable batteries. *Solid State Ion.* **83**, 167-173 (1996).

Figure captions
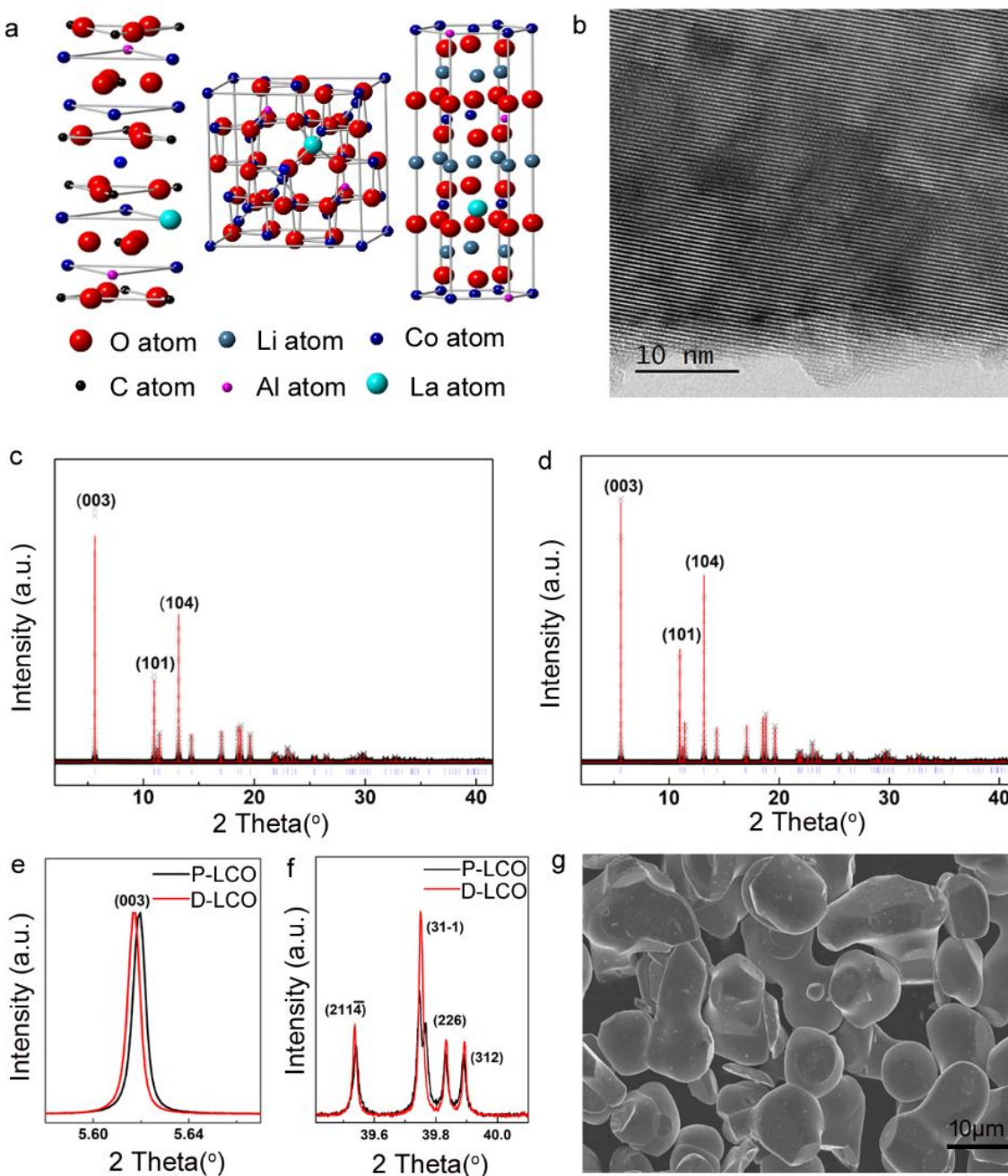
**Figure 1. Ex situ Characterization of D-LCO and P-LCO:** (a) Schematic structures of doped $CoCO_3$ and Co_3O_4, and the final product D-LCO; (b) The HRTEM image of D-LCO; (c)The HRXRD pattern of P-LCO; (d) The HRXRD pattern of D-LCO: $\lambda=0.4593$ Å; (e) Comparison of the (003) peak in P-LCO and D-LCO; (f) Comparison of the characteristic peaks in the HRXRD patterns between 39.4° and 40.2°; (g) The SEM image of D-LCO.
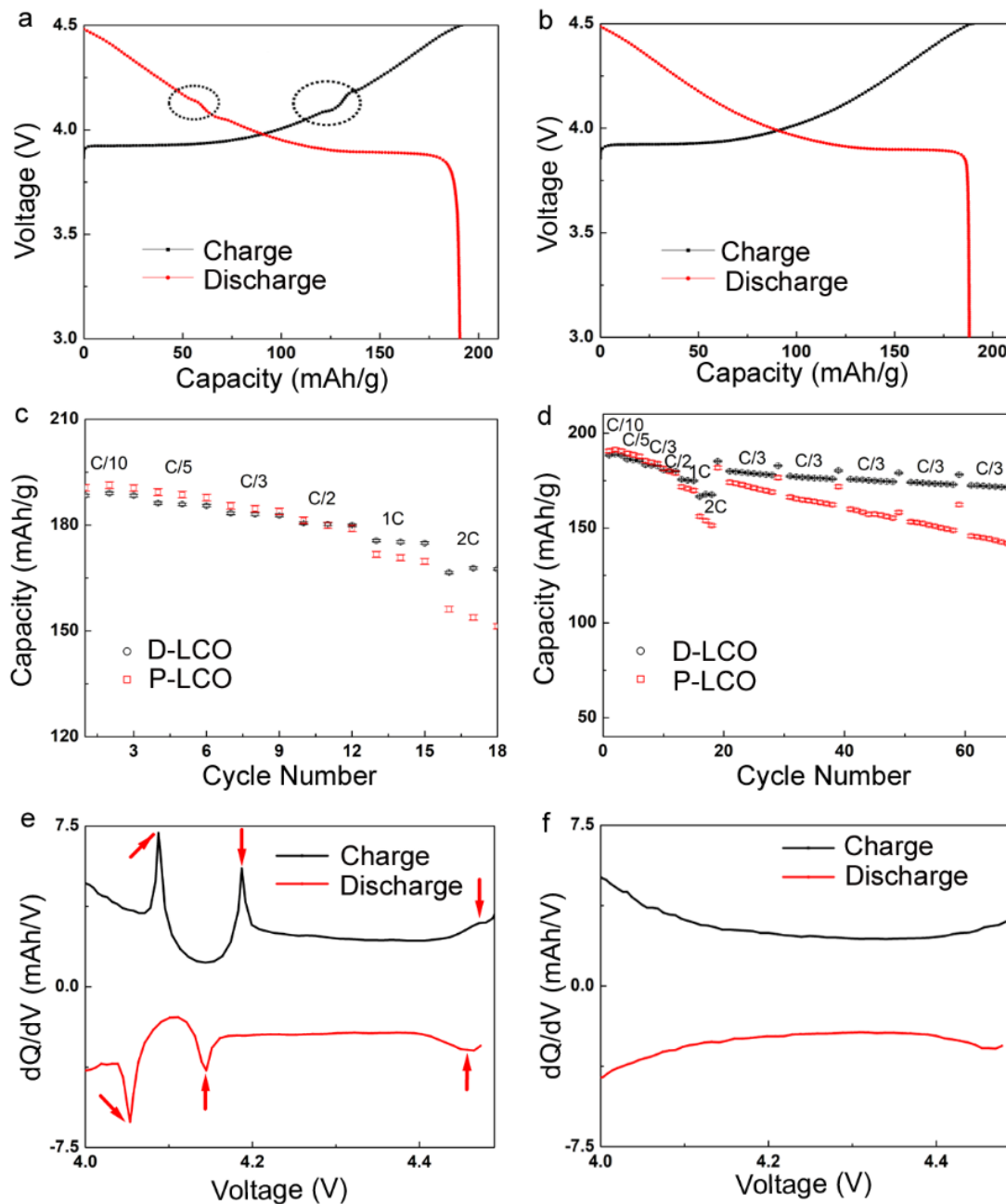
Figure 2. **Electrochemical characterization of the P-LCO and D-LCO:** (a) Charge/discharge voltage profile of P-LCO at C/10(the order/disorder transition was highlighted in the black dash circle); (b) Charge/discharge voltage profile of D-LCO at C/10; (c) Rate performance comparison of P-LCO and D-LCO; (d) Cycling performance comparison of P-LCO and D-LCO; (e) The dQ/dV curve of P-LCO during the formation test (The arrows in the profile indicate three distinct phase transitions respectively); (f) The dQ/dV curve of D-LCO during the formation test.
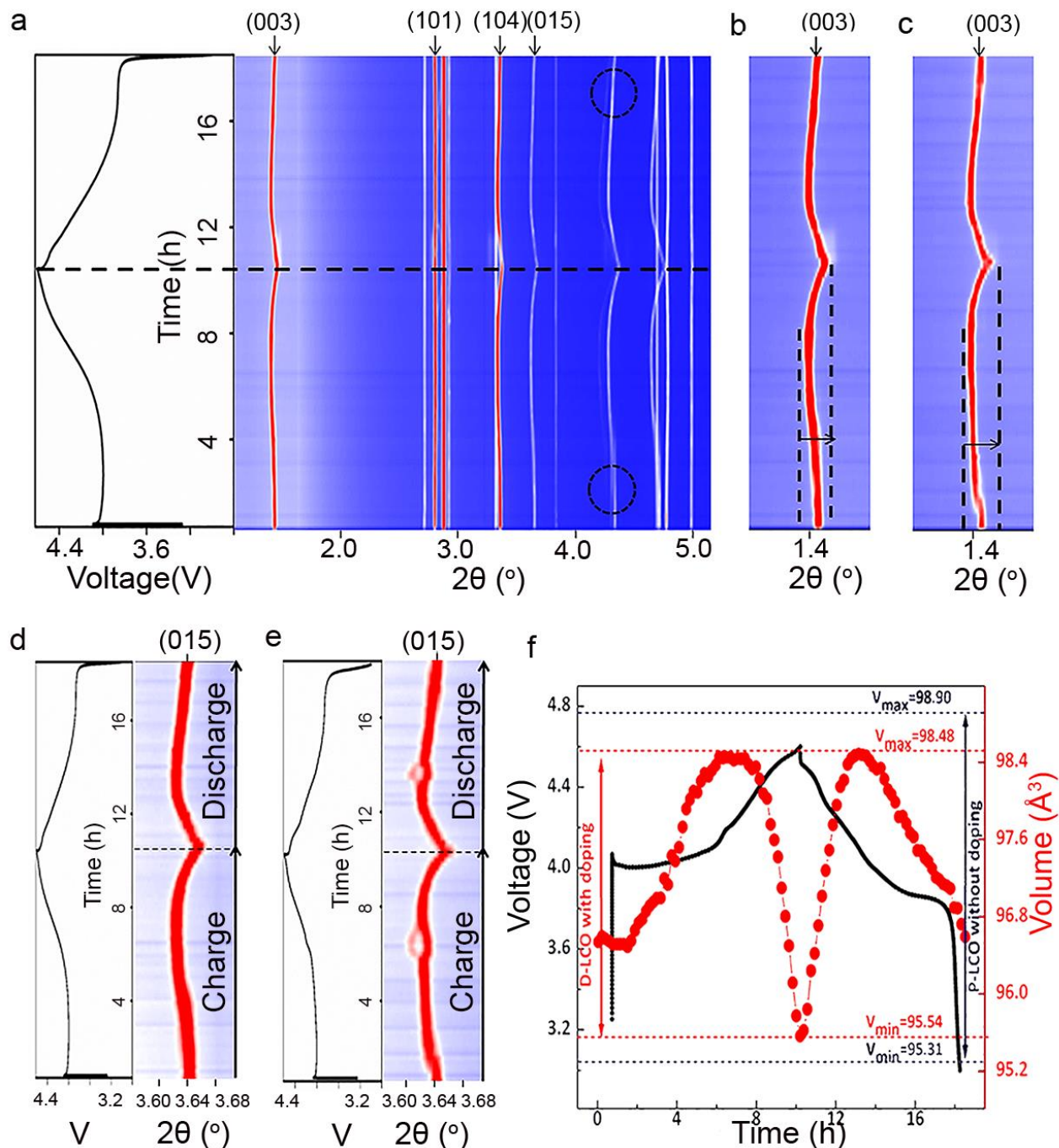
Figure 3. *In situ* **synchrotron HEXRD characterization for D-LCO during the 1**[st]
charge/discharge process: (a)The voltage profile and corresponding contour plot of the XRD
pattern evolution of D-LCO (the insulator-metal transition was highlighted in the black dash circle);
(b) Contour plot of the (003) peaks evolution of D-LCO; (c) Contour plot of the (003) peaks
evolution of P-LCO (the amplitude of the peaks shift was marked by the arrows); (d) Contour plot
of the (015) peaks evolution of D-LCO; (e) Contour plot of the (015) peaks evolution of P-LCO ;
(f) The cell volume evolution process of D-LCO(V_{max}: The maximum cell volume of Li_xCoO_2
during charging; V_{min}: The minimum cell volume of Li_xCoO_2 during charging):.
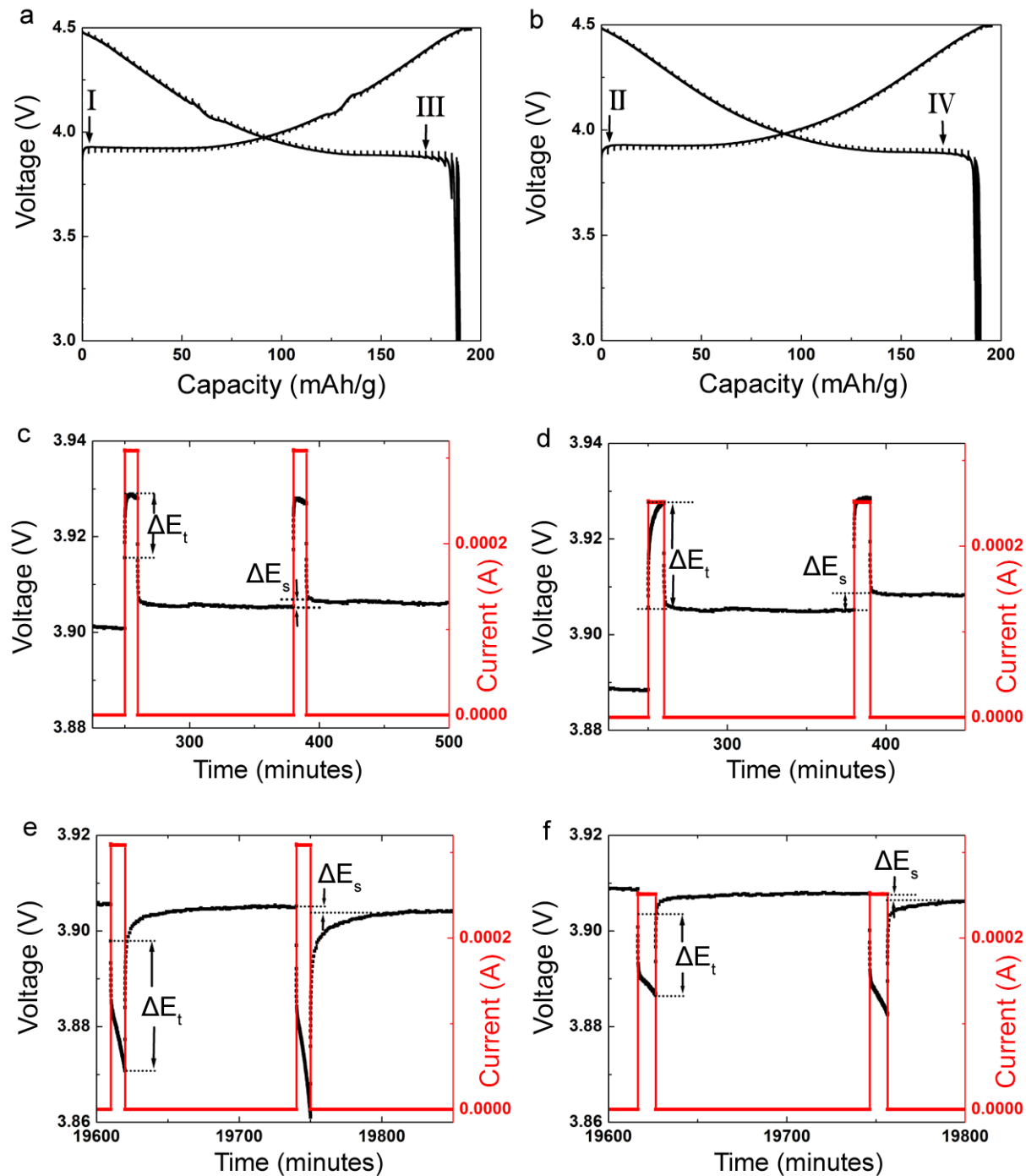
Figure 4. Li ion diffusion coefficient determination of P-LCO and D-LCO via GITT technique: (a) The GITT curve of P-LCO as a function of capacity; (b) The GITT curve of D-LCO as a function of capacity; (c)The GITT curve of P-LCO at the initial charging time mark as "Ⅰ" in Fig.4a; (d) The GITT curve of D-LCO at the initial charging time marked as "Ⅱ" in Fig.4b; (e) The GITT curve of P-LCO at the final discharging time marked as "Ⅲ" in Fig.4a; (f) The GITT curve of D-LCO at the final discharging time marked as "Ⅳ" in Fig.4b. ΔE$_s$ is the change of the steady-state voltage of cell for the related step, and ΔE$_t$ is the total transient voltage change of the cell for the relate step.
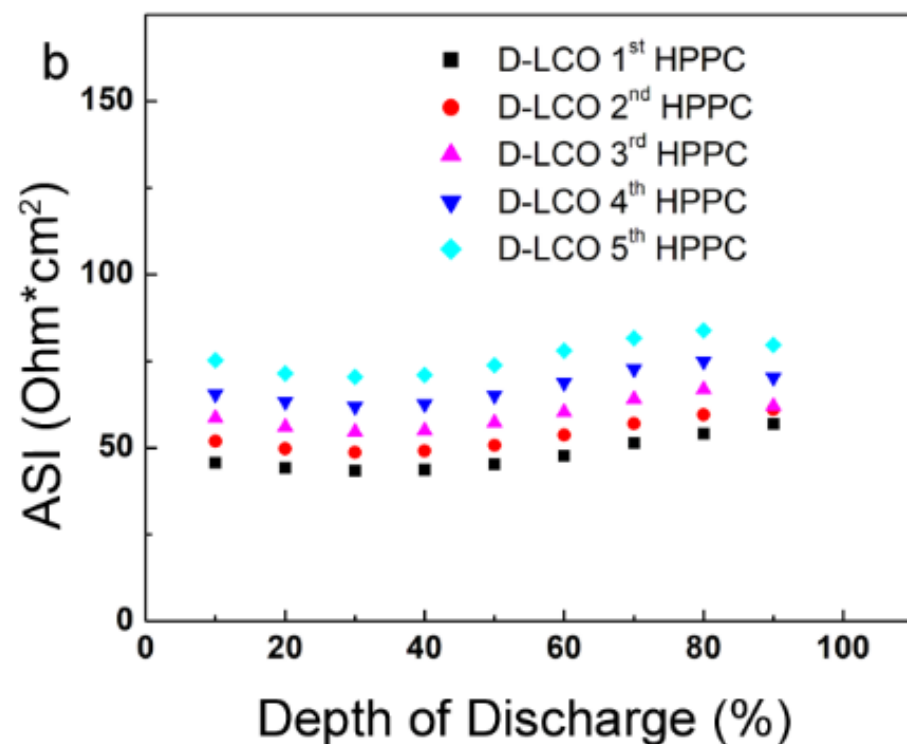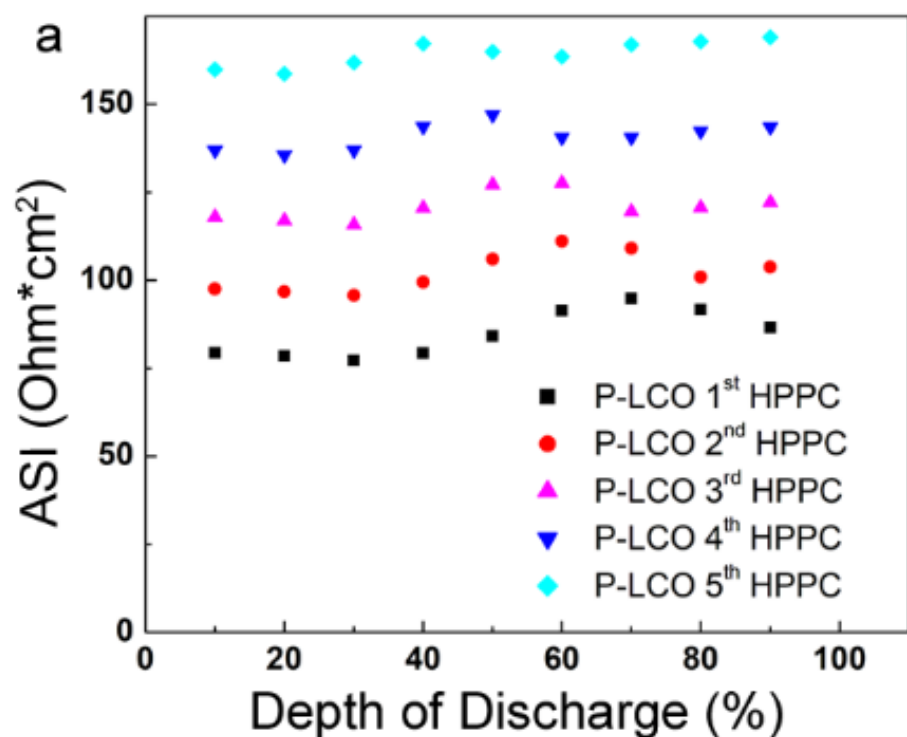
Figure 5. **ASI data of P-LCO and D-LCO determined** *via* **the HPPC**: (a) the ASI pattern of P-LCO in the first 5 cycles; (b) the ASI pattern of D-LCO in the first 5 cycles.
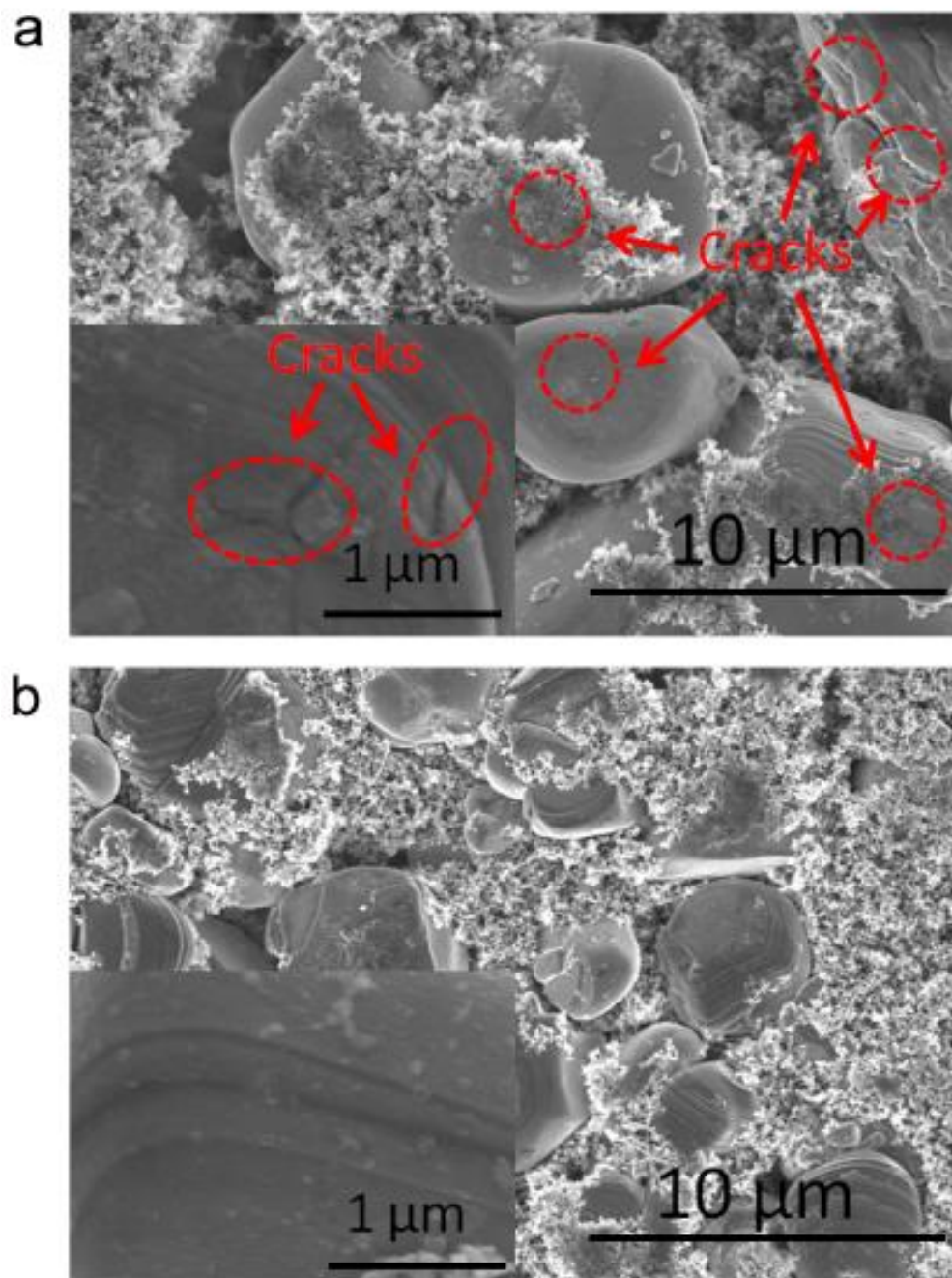
Figure 6. SEM Characterization of P-LCO and D-LCO particles after the cycling test: (a) The SEM images of P-LCO. The insert shows an image with high resolution; (b) The SEM images of D-LCO.